RSC Advances

PAPER

View Article Online
View Journal | View Issue

Cite this: *RSC Adv.*, 2024, **14**, 22159

Insights into structure, morphology and conductivity of the earth-abundant NASICON phosphate, $Na_4MnFe(PO_4)_3$†

Loubna Chayal, [a] Sirine El Arni,[a] Mohamed Saadi, [a] Abderrazzak Assani, [a] Lahcen Bih,[b] Jiwei Ma [c] and Mohammed Hadouchi *[a]

Received 13th May 2024
Accepted 28th June 2024

DOI: 10.1039/d4ra03529a

rsc.li/rsc-advances

Phosphate-based NASICON materials are an excellent candidate for both electrode and solid electrolyte materials in sodium-ion batteries (SIBs). The development of new NASICON materials with higher ionic and electronic conductivities based on low cost and abundant elements is necessary for advancement of SIBs. In this study, we report the structure, morphology and conductivity of the earth-abundant Mn/Fe-based NASICON phosphate $Na_4MnFe(PO_4)_3$. Pure phase powders were synthesized by solution-assisted solid-state reaction, sol–gel and Pechini methods. From refined X-ray diffraction data, the prepared phosphate was found to crystallize in trigonal symmetry with space group $R\bar{3}c$. The effect of synthesis method on microstructure and conductivity was investigated using scanning electron microscopy (SEM), atomic force microscopy (AFM) and impedance measurements. Smaller particle size and regular distribution of the powder was designed using a Pechini route. Impedance measurement showed a notable enhancement in conductivity, from 0.543×10^{-7} to 1.52×10^{-7} S cm^{-1} at 30 °C, when the powder synthesis method was altered from a solution-assisted solid-state reaction to the Pechini route, highlighting the remarkable effect of the synthesis method on conductivity.

1. Introduction

In recent decades, the global energy transition to renewable energy and technological advancements have caused a significant demand for energy storage devices. Rechargeable batteries, particularly lithium-ion batteries (LIBs), play a crucial role in energy storage fields owing to their long cycle life and high energy density.[1–5] Nevertheless, the unequal geographical distribution and skyrocketing price of lithium resources restrict LIB technology from being used indefinitely, especially in large-scale energy storage applications that require a large quantity of active material.[6,7] To overcome this limitation, earth-abundant alternative technologies should be developed. For instance, sodium ion batteries (SIBs) can be a sustainable alternative to LIBs due to the low cost and earth abundance of sodium, as well as their electrochemical properties that are comparable to that of LIBs.[7–9]

In this regard, numerous efforts have been made to develop new efficient components (electrode and electrolyte) for SIBs. NASICON-type polyanionic compounds are one of the most important candidates for use in both electrodes and electrolytes applications in SIBs, thanks to their 3D open framework that provides a large migration channel for Na^+.[10,11] Recently, NASICON phosphates with general formula $Na_{3+x}MnM(PO_3)_4$ (M = transition metal) has been intensively researched, especially as cathode material owing to the environmental-friendly and cost-effective of Mn, as well as the high redox voltage of $Mn^{2+/3+}$ (3.6 V) and $Mn^{3+/4+}$ (4.0 V).[12–18] To date, a variety of Mn–M combinations (M = transition metals) in NASICON structure have been developed such as, $Na_4MnCr(PO_4)_3$,[14] $Na_4MnV(PO_4)_3$,[15] $Na_4MnAl(PO_4)_3$,[16] $Na_3MnTi(PO_4)_3$,[17] and $Na_3MnZr(PO_4)_3$.[18] On the other hand, Fe-based NASICON materials, such as $Na_3Fe_2(PO_4)_3$, have also been largely studied as a promising electrode materials for SIBs because of their high structural stability and low production cost.[19–22] These considerations make the investigation of novel Mn/Fe-based phosphates an attractive idea. Additionally, it is reported that the synergistic effect of Mn–Fe in polyanionic compounds improves thermal stability and generates an increase in the redox potential of Fe.[23,24]

In fact, the development of new electrode materials with higher ionic and electronic conductivities is essential for enhanced the electrochemical properties in SIBs. Various

[a]*Laboratoire de Chimie Appliquée des Matériaux, Centre des Sciences des Matériaux, Faculty of Science, Mohammed V University in Rabat, Avenue Ibn Battouta, BP 1014, Rabat, Morocco. E-mail: m.hadouchi@um5r.ac.ma*

[b]*Laboratory of Sciences and Professions of the Engineer, Materials and Processes Department ENSAM-Meknes Marjane II, Moulay Ismail University, El Mansour, Meknes P.O. Box 15290, Morocco*

[c]*Shanghai Key Laboratory for R&D and Application of Metallic Functional Materials, Institute of New Energy for Vehicles, School of Materials Science and Engineering, Tongji University, Shanghai 201804, China*

† Electronic supplementary information (ESI) available. See DOI: https://doi.org/10.1039/d4ra03529a

strategies were adopted to improve the conductivity in the NASICON structure, *e.g.*, particle design, doping and carbon coating.[10] It is worth noting that the conductivity of the material can also be influenced by different factors, such as the morphology of the particles[25,26] and the presence of secondary phases.[27] In this context, several works were reported on the design of suitable particle morphology and carbon coating *via* various techniques towards high electrochemical performance.[9,25,26]

Based on the above considerations, we report the structural, morphological and conductivity investigations of an earth-abundant Mn/Fe-based NASICON phosphate with 4 Na per formula unit, $Na_4MnFe(PO_4)_3$ (denoted as NMFP). To the best of our knowledge, the synthesis of this compound was reported as single crystal and no structural data were provided.[28] For the first time in this work, we employed three methods, *i.e.*, solution-assisted solid-state reaction, sol–gel and Pechini to synthesize NMFP pure powders and investigated the effect of synthesis methods on the structural, morphological and conduction properties by combining X-ray diffraction (XRD), scanning electron microscopy (SEM), differential scanning calorimetry (DSC), Fourier transform infrared spectroscopy (FT-IR), atomic force microscope (AFM) and impedance spectroscopy.

2. Experimental section

2.1. Materials preparation

2.1.1 NMFP powder synthesis. NMFP was prepared by a solution-assisted solid-state reaction, a simple sol–gel and Pechini methods. Na_2NO_3 (99.4%, VWR Chemicals), $MnCO_3$ (99.9%, Alfa Aesar), $Fe(NO_3)_3\cdot 9H_2O$ (≥99.0% AnalaR NORMAPUR) and $NH_4H_2PO_4$ (99.9%, Acros Organics) are used as starting reagents in 2 : 1 : 1 : 3 molar ratios, respectively. In each method, firstly, a solution A was prepared from a mixture of Na_2NO_3, $MnCO_3$, and $Fe(NO_3)_3\cdot 9H_2O$ dissolved in 60 ml of distilled water with 8 ml of HNO_3 and kept 1 h in stirring under heating at 60 °C.

For the solution-assisted solid-state reaction, solution B was prepared by dissolving $NH_4H_2PO_4$ in 50 ml of distilled water and added to the fist solution. The obtained solution was stirred at 80 °C for 3 h and heated overnight to evaporate water. The resulting precipitate was dried at 120 °C for 6 h and calcined at 400 °C and 700 °C for 24 h each in an air atmosphere, with a heating rate of 10 °C min^{-1}. Subsequent to each calcination step, the powder was cooled and reground in an agate mortar.

In the case of sol–gel method, a second solution B′ was prepared by dissolving $NH_4H_2PO_4$ and citric acid with the molar ratio (Na^+, Mn^{2+}, Fe^{3+}): citric acid (≥99%, VWR Chemicals) = 1 : 1 in 50 ml of distilled water. Then, the solution A + B′ was stirred at 80 °C for 3 h. After that, the final solution was heated overnight to form a gel. The obtained gel was dried at 120 °C for 6 h and underwent the same heat treatment applied for the solution-assisted solid-state method.

For the Pechini route, in addition to the solution B′ as prepared in case of sol gel, another solution C was prepared by dissolving ethylene glycol (≥99.5%, Panreac) in 10 ml of distilled water in molar ratio ethylene glycol : citric acid = 4 : 1. The mixed solution A + B′ + C was stirred at 80 °C until a solid gel was formed. The obtained gel was dried at 120 °C for 24 h before being sintered under the same temperatures as those outlined in the solution-assisted solid-state method.

2.1.2 Pellets preparations

For the measurement of the complex impedance, a solution with 2 wt% PVA was prepared, each prepared powder was ground in agate mortar with 20 wt% of this solution as a binder and pressed into pellets of 13 mm in diameter with a pressure of 8 MPa for 3 min. Then, the pressed pellets were sintered at 500 and 710 °C for 4 and 12 h, respectively, with a heating rate of 5 °C min^{-1}. The obtained pellets were covered with silver lacquer to guarantee good electrical contact between the pellet and the electrodes.

2.2. Materials characterization

The purity of the synthesized powders was analyzed by X-ray diffraction (XRD) at room temperature, using a Rigaku SmartLab X-ray Diffractometer operating in the 2θ range of $10° \leq 2\theta \leq 100°$ with a 0.02° step and a 5° min^{-1} scan rate. The obtained powder diffraction patterns were analyzed and refined by Rietveld refinement approach using FullProf Program,[29] based on the crystallographic information file (CIF) of $Na_4MnV(PO_4)_3$.[8] The structural visualization was carried out using Diamond software.[30] The morphology and the chemical composition of the synthesized samples were observed and analyzed using a scanning electron microscope (QUATTRO S-FEG-Thermofisher scientific) coupled with an energy-dispersive X-ray spectroscopy (EDS) analyzer. The Archimedean method was used to calculate the density of the sintered pellets using distilled water as a suspension medium. The surfaces of the pellets were observed using Atomic Force Microscope (CoreAFM). The infrared spectroscopy spectra of the powder samples were obtained using FT-IR spectrometer (PerkinElmer RX-I model), covering a frequency range of 400–4000 cm^{-1}. Differential scanning calorimetry (DSC) measurement was carried out by Shimadzu DSC-60 Plus within a 45–300 °C temperature range in the atmosphere with a heating rate of 10 °C min^{-1}.

2.3 Impedance measurements

The impedance measurement was carried out at different temperatures (RT-150 °C) in the frequency range from 1 Hz to 1 MHz using Solartron analytical Modulab Xm MTS device coupled to Linkam cell, and the data was fitted using the ZView software. The ionic conductivity (σ) and the activation energy (E_a) were derived from impedance data using eqn (1) and (2), respectively.

$$\sigma = \frac{L}{RS} \quad (1)$$

where L = pellet thickness, S = surface area of the electrode placed on the pellet and R = resistance value.

$$\sigma = A \exp\left(\frac{-E_a}{KT}\right) \quad (2)$$

where A = pre-exponential factor, T = absolute temperature, K = Boltzmann constant.

3. Results and discussion

3.1 Structural and morphological description

The NMFP samples prepared by solution-assisted solid-state reaction, sol–gel and Pechini routes denoted as NMFP/SS, NMFP/SG and NMFP/P, respectively, crystallize in a NASICON structure with $R\bar{3}c$ space group. The Rietveld refined powder X-ray diffractograms of NMFP/SS, NMFP/SG and NMFP/P are illustrated in Fig. 1a–c. The Rietveld refinement of the three samples exhibits a good correlation between the calculated and the experimental XRD patterns with good weighted profile *R*-factor, which confirms the formation of the Trigonal NASICON pure phase with $R\bar{3}c$ space group. A negligible difference is observed between the obtained crystallographic data of the three powders. The refinement details of the three powder XRD patterns are listed in Table 1.

The crystal structure created from CIF file of NMFP/SG is illustrated in Fig. 1d. This structure is built by edge-sharing MnO_6/FeO_6 octahedra and PO_4 tetrahedra forming a basic constituent known as 'lantern unit', leading to the 3D-dimensional open framework. In this structure, Na atoms occupied two types of interstitial sites with different oxygen coordination environments: Na1 site in the 6*b* Wyckoff position (100% occupied) with sixfold coordination and Na2 site in 18*e* Wyckoff position (100% occupied) with eightfold coordination. Fe and Mn atoms occupy octahedral environment by sharing the 12*c* Wyckoff position with 50% occupancy per each. The bond-valence model (BVS) (Brown & Altermatt)[31] was applied to all three samples. The BVS values calculated for Na1, Na2, and P1 are approximately 1.1, 0.9, and 5.0, respectively, which are close to the expected oxidation states, *i.e.*, Na^{1+} and P^{5+}. The mixed Mn/Fe site shows a total BVS value of 2.7 + 2.5 = 5.2, which is close to the sum of Mn^{2+} and Fe^{3+} oxidation states. However, to accurately confirm the exact oxidation state of each element, further characterization techniques are required, such

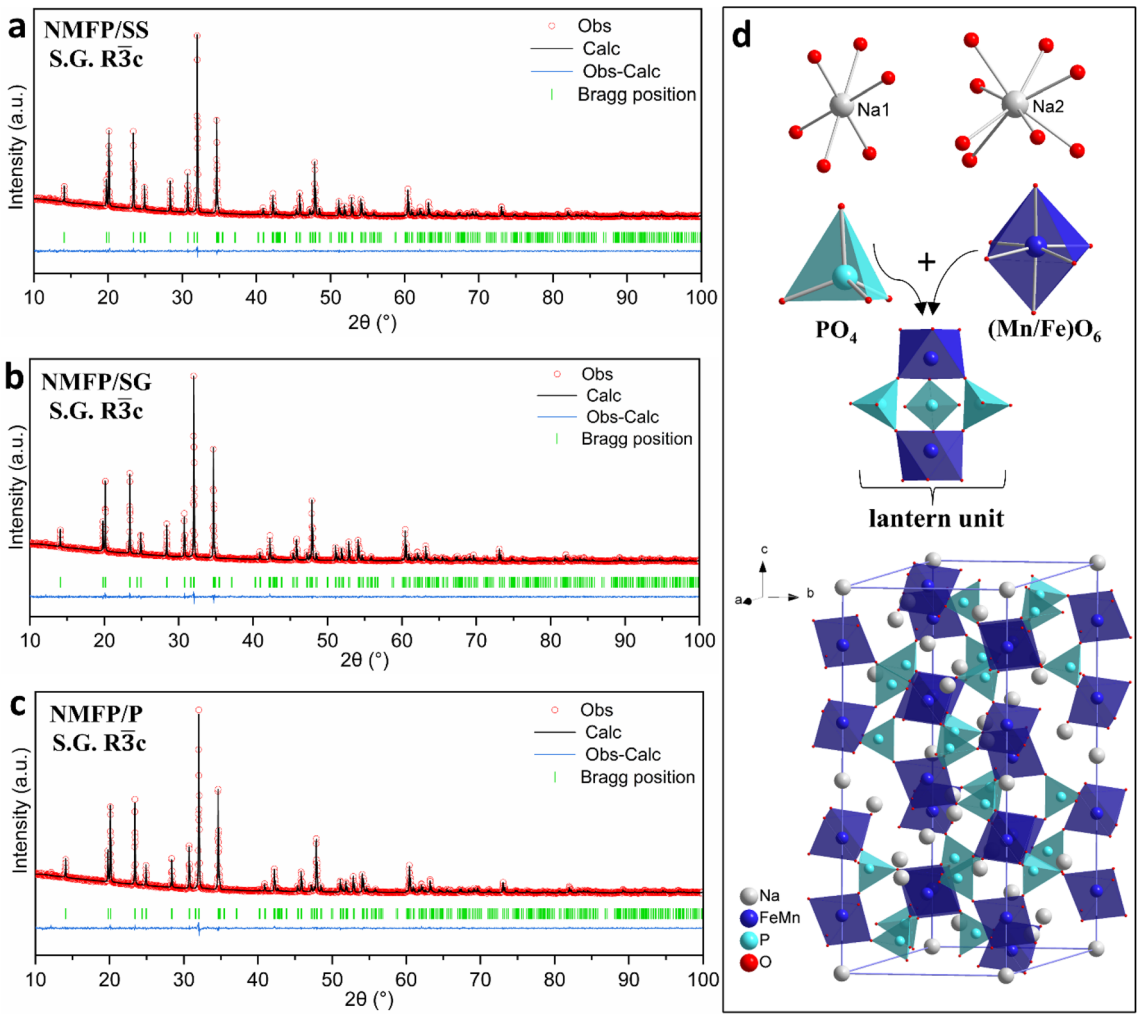

Fig. 1 (a–c) Rietveld refinement of NMFP powders, (d) visual representation of Na1, Na2, Mn/Fe and P atoms environments and NMFP unit cell.

Table 1 Rietveld refinement data of NMFP synthesized by different methods

Crystal data			
Synthesis method	SS	SG	P
Chemical formula	$Na_4MnFe(PO_4)_3$	$Na_4MnFe(PO_4)_3$	$Na_4MnFe(PO_4)_3$
M_r (g mol^{-1})	487.66008	487.66008	487.66008
Crystal system, space group	Trigonal, $R\bar{3}c$	Trigonal, $R\bar{3}c$	Trigonal, $R\bar{3}c$
Temperature (K)	289	289	289
a, c (Å)	8.96603 (7), 21.4326 (2)	8.96068 (6), 21.44306 (18)	8.96746 (9), 21.4345 (3)
V (Å^3)	1492.13 (2)	1491.07 (2)	1492.74 (3)
Z	6	6	6
Radiation type	X-ray, Cu Kα ($\lambda = 1.5406$ Å)		
Data collection			
Diffractometer	Rigaku SmartLab		
2θ values (°)	$2\theta_{min} = 10.01$ $2\theta_{max} = 100.01$ $2\theta_{step} = 0.02$		
Refinement			
R factors and goodness of fit	$R_p = 2.354$, $R_{wp} = 2.987$, $R_{exp} = 2.689$, $R_{Bragg} = 4.432$, $\chi^2 = 1.234$	$R_p = 2.376$, $R_{wp} = 3.052$, $R_{exp} = 2.704$, $R_{Bragg} = 5.062$, $\chi^2 = 1.273$	$R_p = 2.346$, $R_{wp} = 2.986$, $R_{exp} = 2.686$, $R_{Bragg} = 4.343$, $\chi^2 = 1.235$
No. of parameters	94	94	94
No. of data points	4501	4501	4501

as XPS measurements. The details of atomic positions, isotropic displacement parameters and BVS calculation of NMFP materials are given in Table 2. The selected bond distances and the atomic angles are summarized in Table S1.† Similar to other NASICON phosphates, Na(2)–O distances are found to be higher than the Na(1)–O distances, leading to an easier extraction of Na^+ from the Na2 site compared to the Na1 during the redox reaction.[15,32]

The surface morphology and elemental composition of NMFP/SS, NMFP/SG and NMFP/P powders were analyzed by electron microscopy (SEM) and energy dispersive X-ray spectroscopy (EDS). The grain size distribution of the powders is shown in Fig. 2a, the morphology of NMFP/SS, NMFP/SG and NMFP/P powders indicates the formation of nearly round-shaped and polygonal grains. From the histograms plotted in Fig. S1a† determined through analysis with the ImageJ software, a significant difference in particle size can be observed between the three powders. The grain size of NMFP/SS powder is irregular, characterized by the presence of larger particles with sizes approaching 8 μm and smaller grains with equivalent diameters ranging from about 1 to 6 μm. While the NMFP/SG and NMFP/P powders have uniform rounded-shape particles with sizes of around 1–4 μm and average grain sizes of 2.45 and 1.81 μm for NMFP/SG and NMFP/P respectively. This

Table 2 Atomic positions, isotropic displacement parameters (Å^2) and BVS calculation of NMFP synthesized by different methods

	Method	x	y	z	U_{iso}	Occ. (<1)	BVSum
Na1	SS	0.00000	0.00000	0.00000	0.020 (2)		1.143 (6)
	SG	0.00000	0.00000	0.00000	0.017 (2)		1.105 (5)
	P	0.00000	0.00000	0.00000	0.018 (3)		1.118 (5)
Na2	SS	−0.3333	−0.0267 (5)	0.08330	0.0340 (16)		0.952 (5)
	SG	−0.3333	−0.0277 (5)	0.08330	0.0363 (15)		0.952 (4)
	P	−0.3333	−0.0275 (5)	0.08330	0.0310 (16)		0.949 (5)
Fe	SS	0.00000	0.00000	0.14962 (8)	0.0087 (8)	0.50000	2.554 (13)
	SG	0.00000	0.00000	0.14932 (8)	0.0102 (8)	0.50000	2.567 (12)
	P	0.00000	0.00000	0.14940 (9)	0.0087 (9)	0.50000	2.554 (13)
Mn	SS	0.00000	0.00000	0.14962 (8)	0.0087 (8)	0.50000	2.777 (14)
	SG	0.00000	0.00000	0.14932 (8)	0.0102 (8)	0.50000	2.791 (13)
	P	0.00000	0.00000	0.14940 (9)	0.0087 (9)	0.50000	2.777 (14)
P	SS	−0.3333	−0.3674 (3)	0.08330	0.0118 (12)		5.015 (30)
	SG	−0.3333	−0.3682 (3)	0.08330	0.0095 (11)		5.097 (30)
	P	−0.3333	−0.3676 (3)	0.08330	0.0114 (13)		5.067 (31)
O1	SS	0.1951 (5)	0.2083 (5)	0.19238 (16)	0.0129 (16)		
	SG	0.1963 (5)	0.2084 (5)	0.19292 (17)	0.0180 (16)		
	P	0.1962 (5)	0.2075 (5)	0.19263 (18)	0.0180 (18)		
O2	SS	0.1857 (4)	0.0149 (6)	0.0844 (2)	0.0085 (13)		
	SG	0.1853 (4)	0.0148 (5)	0.0853 (2)	0.0086 (12)		
	P	0.1857 (4)	0.0144 (6)	0.0848 (2)	0.0087 (13)		

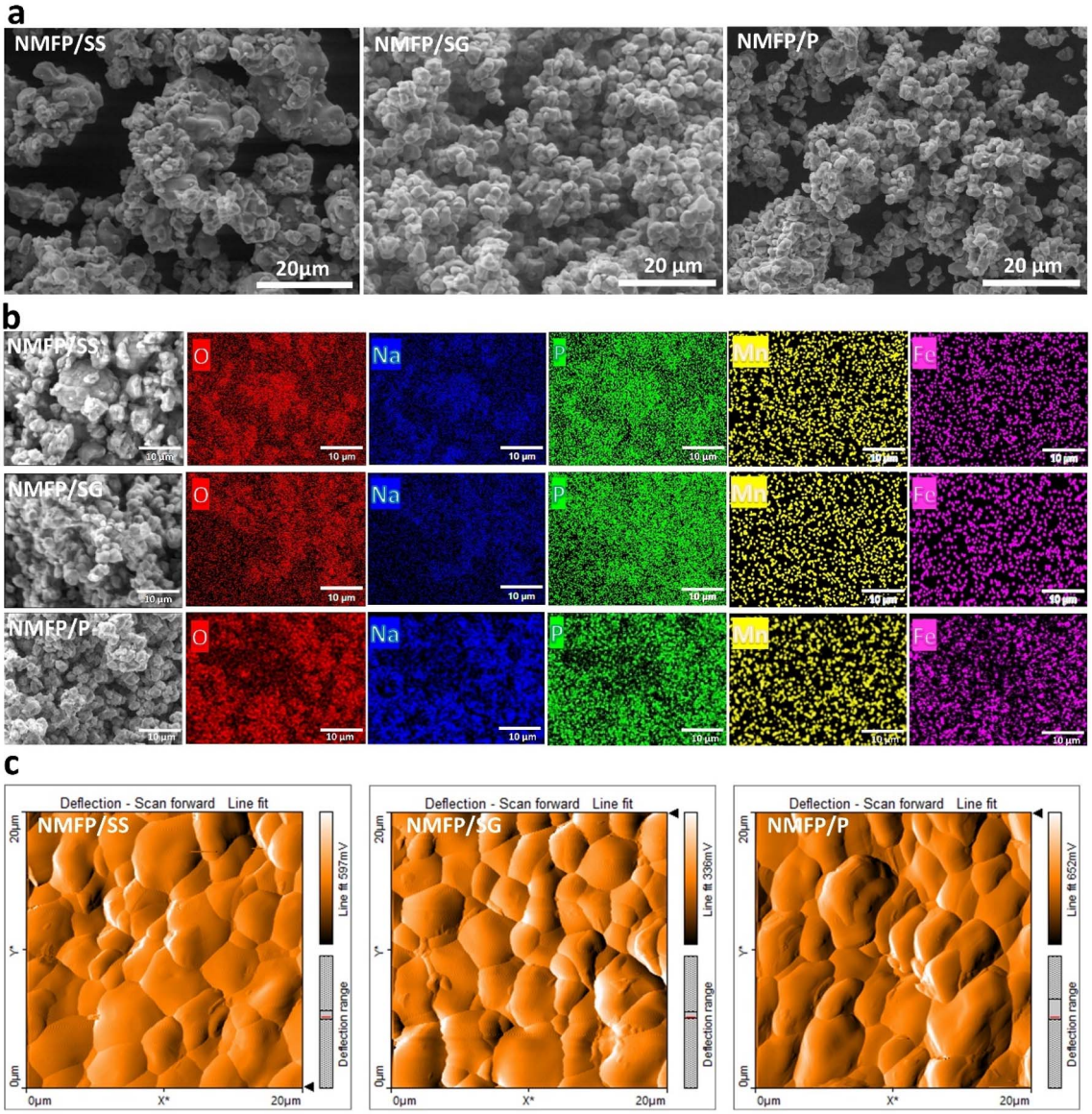

Fig. 2 (a) SEM images and (b) EDS elemental mapping images of NMFP powders. (c) AFM surface images of NMFP pellets sintered at 710 °C.

Table 3 Density of NMFP pellets

Pellets	Theoretical density (g cm^{-3})	Relative density (%)
NMFP/SS	3.256	92.260
NMFP/SG	3.259	93.568
NMFP/P	3.255	97.907

observation explained by the impact of the synthesis method on particle size. The sol–gel and the Pechini methods tend to produce smaller and regular grains than the solid-state method.[33,34] The EDS mapping presented in Fig. 2b confirms the homogeneous distribution of Na, Mn, Fe in the three powders. The EDS spectra (Fig. S2†) of the different powders confirm the existence of Na, Fe, Mn, P and O elements with atomic ratios very near to expected stoichiometric composition, *i.e.*, Mn/Fe ratios are 1.14, 1.16, 1.15 for NMFP/SS, NMFP/SG and NMFP/P, respectively, which is in good agreement with powder diffraction data.

Fig. 2c, shows the surface images of pellets sintered at 710 °C using Atomic Force Microscope (AFM). The theoretical and relative density determined by Rietveld refinement and Archimedean method are listed in Table 3. All the samples show a high relative density (>90%). The NMFP/P pellet possess the highest density of ~97.91%, while NMFP/SS pellet has the lower density of ~92.26%. These findings are further supported by AFM images, where the grains appear more densified passing from NMFP/SS to NMFP/P pellet. The average grain size of sintered pellets was determined using ImageJ software based on AFM images (Fig. S1b†). Values of 3.89, 3.33, and 3.47 µm were obtained for the NMFP/SS, NMFP/SG and NMFP/P pellets, respectively. The observed increase in grain size compared to

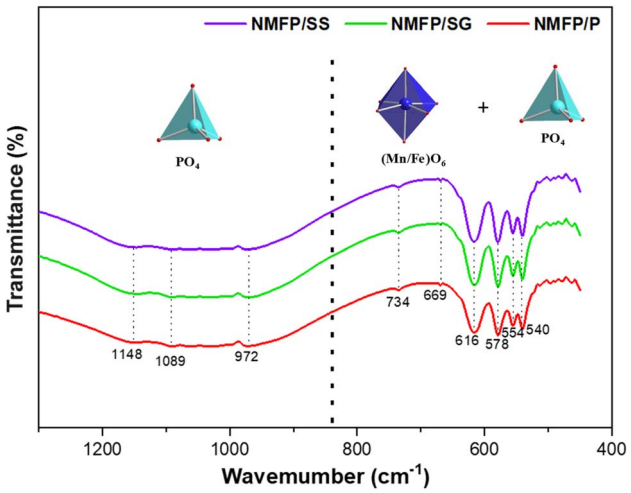

Fig. 3 FT-IR spectrum of the NMFP synthesized by the three routes.

the pristine powders is explained by particle growth with heat treatment at 710 °C.

3.2. FT-infrared spectroscopy

The FTIR spectra of the three powders are presented in Fig. 3. It appears that all samples exhibit FTIR spectra with identical band positions and similar intensities. The absorption bands at ~554, 669 and 734 cm^{-1} can corresponds to the bending/stretching of Mn/Fe–O bond in Mn/FeO_6 octahedra.[35,36] The rest of the bands observed around 970–1200 cm^{-1} and 400–600 cm^{-1} corresponds to $[PO_4]^{3-}$ stretching: ν_3 (PO_4) = 1148 cm^{-1}, 1089 cm^{-1}; ν_1 (PO_4) = 972 cm^{-1}; ν_4 (PO_4) = 616 cm^{-1}, 578 cm^{-1}, 540 cm^{-1}.[35,37,38] These results are in good agreement with the reported literature of NASICON phosphates.[35]

3.3 Impedance study

To investigate the impact of synthesis method on the electrical properties of NMFP compound, impedance spectroscopy was performed on the three pellets. Fig. 4a shows the complex impedance curves of NMFP/SS, NMFP/SG and NMFP/P pellets at 30 °C. The Nyquist plot of the three samples exhibits three different regions depending on the frequency. The first region at a higher frequency shows a depressed semicircular arc corresponding to the grain response, represented by sub-equivalent circuit resistance (R_G)/constant phase element (CPE1). The second region at intermediate frequency shows an incomplete semicircle representing the grain boundary behavior, described by a sub-equivalent circuit resistance (R_{GB})/constant phase element (CPE2). This region is clearly

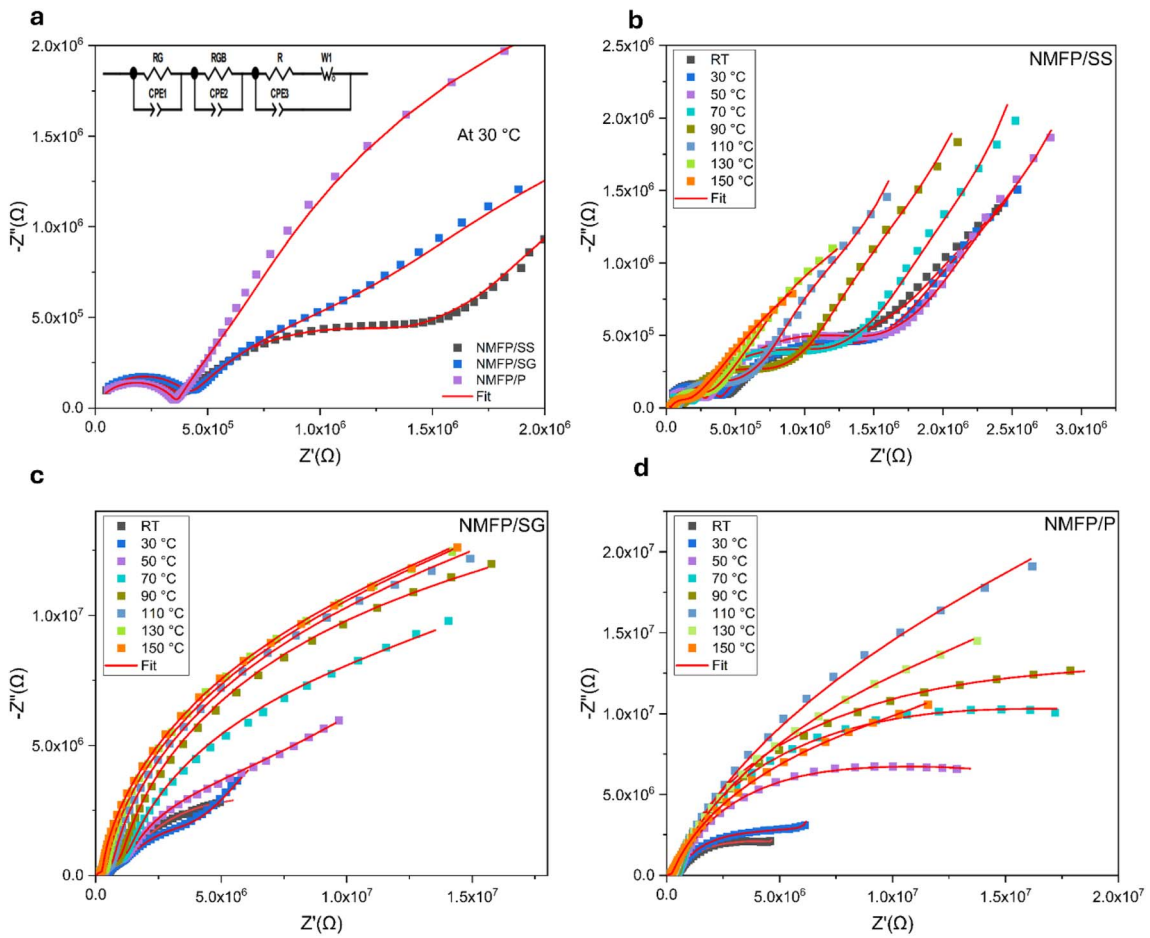

Fig. 4 Nyquist curves of NMFP/SS, NMFP/SG and NMFP/P pellets (a) at 30 °C and (b–d) at different temperature.

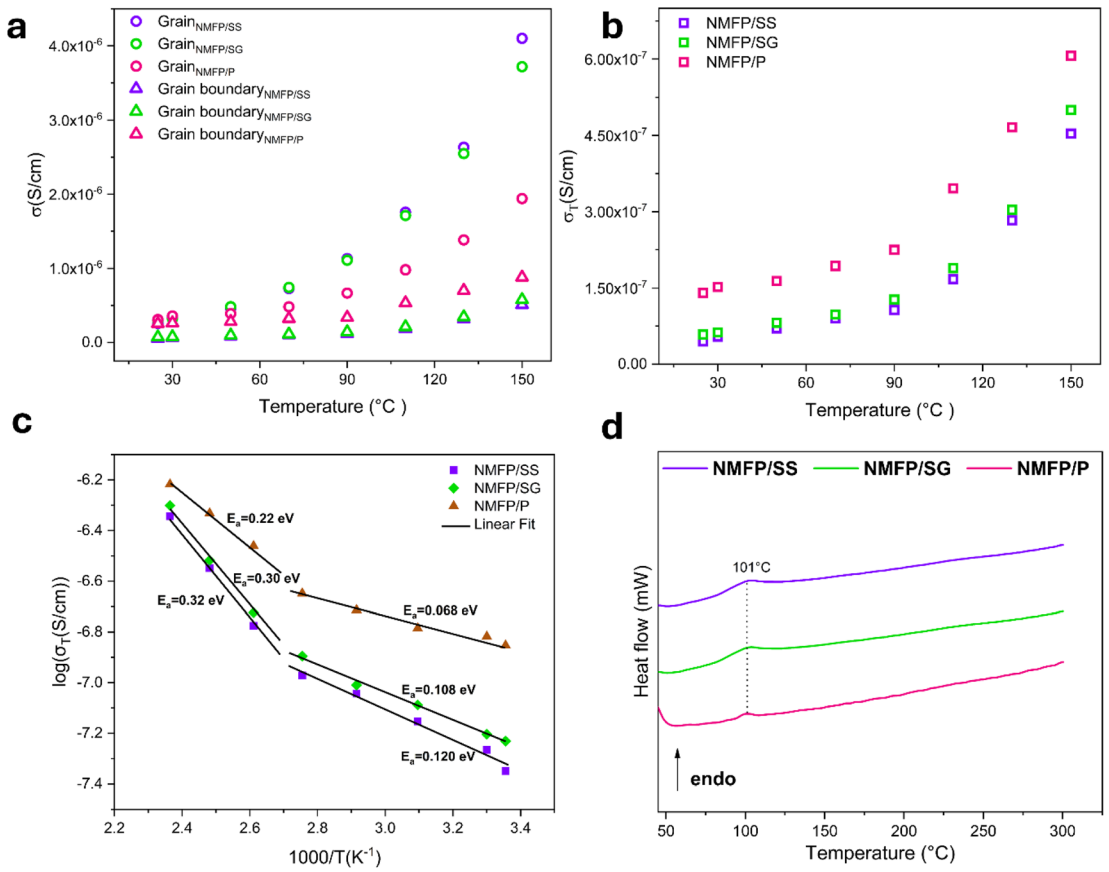

Fig. 5 (a, b) Grain, grain boundary and total conductivities of NMFP pellets as a function of temperature. (c) Arrhenius plots of NMFP pellets. (d) DSC measurement of NMFP samples from 45 to 300 °C.

distinguishable in the case of NMFP/SS and NMFP/SG curves compared with NMFP/P curve. The last region at lower frequency shows a curved spike, describes the sample-electrode interface polarization process. The equivalent sub-circuit that fits the last region is a bit complex, is formed by a resistance (R) in series with a Warburg element (W_1) and in parallel with a constant phase element (CPE3). The R resistance corresponds to the metallic electrode resistance. The Warburg element (W_1) indicates the presence of blocking diffusion due to the Ag-paste that works as a blocking electrode preventing Na^+ ions from crossing the interface. The third constant phase element (CPE3) reflects the impedance response arising from the distribution of ionic and electronic polarization processes occurring at the pellet-electrode interface.[39] This equivalent sub-circuit confirms that the conductivity of the materials is a mixture of an ionic and electronic nature.[40] The total equivalent circuit used to fit the impedance spectra is inset in Fig. 4a.

For the three simples, as the temperature increases (Fig. 4b–d), the diameter of the semicircle at high frequency decreases and the incomplete semicircle at intermediate frequency shifts to lower value of Z'. Additionally, the semicircle at high frequency appears smaller than the incomplete semicircle at lower frequency. These observations indicate the diminution of R_G and R_{GB} when the temperature increases, as well as the higher values of R_{GB} compared to R_G. The R_G is estimated from the intercept of the semicircle arc at high frequency on the real impedance axes. The values of R_G and R_{GB} were obtained by fitting the impedance data using the equivalent circuit.

The grain, grain boundary and total conductivities of the three samples are calculated using the eqn (1) as shown in Fig. 5a and b. In the temperature range of RT-50 °C, the three samples exhibit nearer grain conductivity values (Fig. 5a), which indicate that the synthesis method is not the main factor governing grain conductivity, but the crystal structure and charge

Table 4 Conductivities of NMFP pellets at 30 °C and the activation energies

Pellets	σ_G (S cm^{-1}) $\times 10^{-7}$	σ_{GB} (S cm^{-1}) $\times 10^{-7}$	σ_T (S cm^{-1}) $\times 10^{-7}$	$E_{aRT\leq T\leq 90°C}$ (eV)	$E_{a90<T\leq 150°C}$ (eV)
NMFP/SS	3.370	0.647	0.543	0.120 ± 0.009	0.32 ± 0.02
NMFP/SG	3.230	0.760	0.626	0.108 ± 0.005	0.30 ± 0.03
NMFP/P	3.590	2.640	1.520	0.068 ± 0.006	0.22 ± 0.02

carrier concentration.[34] As the temperature increases, a noticeable difference is observed between the grain conductivities of the pellets, NMFP/P shows the lower value and NMFP/SS shows the higher value. The lower grain conductivity value of NMFP/P pellets at higher temperature comparing to NMFP/SS and NMFP/SG pellets can be explained by the collision between charge carrier due to their fast kinetic speed.[41] In contrast, the temperature dependence of grain boundary conductivity exhibited consistent trends for the three pellets in the temperature range RT-150 °C (Fig. 5a), which NMFP/P displayed the highest value depending on relative density. At 30 °C as presented in Table 4, grain boundary conductivity of NMFP/P pellet (97.9% relative density) shows value of 2.64×10^{-7} S cm^{-1} three times higher than that of NMFP/SG (0.760×10^{-7} S cm^{-1} with $\simeq$93.6% relative density) and four times higher than that of NMFP/SS (0.647×10^{-7} S cm^{-1} with $\simeq$92.3% relative density), revealing a significant correlation between pellet relative density and grain boundary conductivity. The higher density can offer more transfer pathways for charge carriers migration through grain boundaries.[42] The total conductivity (Fig. 5b) of the three pellets follows the same behavior of grain boundary conductivity and shows value of 0.543×10^{-7}, 0.626×10^{-7} and 1.520×10^{-7} S cm^{-1} for NMFP/SS, NMFP/SG and NMFP/P, respectively, at 30 °C (Table 4). In fact, the total conductivity of NMFP/P pellet is significantly higher than that of NMFP/SS and NMFP/SG in all temperature range RT-150 °C. This suggests the predominant role of grain boundary conductivity in governing the total conductivity of our material. It was previously reported that the total conductivity of NASICON material is often governed by the grain boundary conductivity.[43] Therefore, the conductivity of our NASICON samples is significantly affected by the synthesis conditions.

The Arrhenius plot of the total conductivities of the three samples is presented in Fig. 5c. The activation energy of the three samples were calculated using eqn (2). In all cases, two linear regions are present, indicating that each sample is characterized by two activation energies. This behavior can be explained by the presence of a phase transition in the NMFP structure.[44,45] DSC curves of NMFP/SS, NMFP/SG and NMFP/P powders measured between 45–300 °C (Fig. 5d) show the presence of an endothermic weak peak at around 95–102 °C. This peak can be associated with unidentified polymorphic transition. Based on a previous report, R. R. Samigullin *et al.* claimed a temperature-dependence polymorphic transition at 55–65 °C in NASICON $Na_4VMn(PO_4)_3$.[46] Consequently, the DSC measurement supports the activation energy behavior, but further temperature-dependent XRD studies are required to reveal more structural information. In the lower temperature region, NMFP/SS, NMFP/SG and NMFP/P samples present activation energies of 0.12, 0.108, 0.068 eV, respectively, associated to the rhombohedral phase. Where, at higher temperatures, all three samples present an activation energy three times higher than that of the first region (Table 4). In both regions, NMFP/P pellets show the lowest activation energy values, *i.e.* 0.068 and 0.22 eV for the first and second regions respectively. Notably, lower than those typically reported in the literature for the NASICON structure.[47] Furthermore, the observed increase in activation energy at high temperature probably indicated that the remarkable phase transition leads to a phase where Na^+ ions become minimally mobile because of their order in the structure of the polymorph as in monoclinic NASICON.[47,48]

4. Conclusion

In summary, $Na_4MnFe(PO_4)_3$ NASICON compound with $R\bar{3}c$ space group was successfully synthesized by solution-assisted solid-state reaction, sol–gel and Pechini methods. The investigation of synthesis-related effects on microstructure and conductivity was reported. The Pechini method led to smaller particle size, resulting in a high-density pellet. The higher density achieved by this method contributes significantly to improving the total conductivity, especially the grain boundary conductivity. Total conductivity value of 1.52×10^{-7} S cm^{-1} was obtained for NMFP/P samples at 30 °C with the smaller activation energy of 0.068 eV in the temperature range of RT-90 °C. The lower activation energy obtained at temperatures below 90 °C and lower cost of the precursor materials can make this NASICON phosphate as a promising candidate for future energy storage applications.

Data availability

The data supporting this article have been included as part of the ESI.†

Author contributions

Loubna Chayal: data curation, formal analysis, investigation, visualization, writing –original draft. Sirine El Arni: data curation, formal analysis. Mohamed Saadi: supervision, validation, project administration, resources. Abderrazzak Assani: formal analysis, validation. Lahcen Bih: data curation, validation, resources. Jiwei Ma: data curation, validation, resources. Mohammed Hadouchi: data curation, conceptualization, supervision, validation, project administration, resources, writing – review & editing.

Conflicts of interest

There are no conflicts of interest to declare.

Acknowledgements

This work is carried out with the support of the CNRST as part of the "PhD-ASsociate Scholarship – PASS" Program. The authors would like to thank the faculty of science, Mohammed V University in Rabat for X-ray data collection.

References

1 B. Rowden and N. Garcia-Araez, Estimating lithium-ion battery behavior from half-cell data, *Energy Rep.*, 2021, **7**, 97–103.

2 P. K. Nayak, L. Yang, W. Brehm and P. Adelhelm, From Lithium-Ion to Sodium-Ion Batteries: Advantages, Challenges, and Surprises, *Angew. Chem., Int. Ed.*, 2018, **57**(1), 102–120.

3 H. Kim, G. Yoon, I. Park, J. Hong, K. Y. Park, J. Kim, *et al.*, Highly Stable Iron- and Manganese-Based Cathodes for Long-Lasting Sodium Rechargeable Batteries, *Chem. Mater.*, 2016, **28**(20), 7241–7249.

4 Y. Liu, J. Li, Q. Shen, J. Zhang, P. He, X. Qu, *et al.*, Advanced characterizations and measurements for sodium-ion batteries with NASICON-type cathode materials, *eScience*, 2022, **2**(1), 10–31.

5 M. Hadouchi, T. Koketsu, Z. Hu and J. Ma, The origin of fast-charging lithium iron phosphate for batteries, *Battery Energy*, 2022, **1**(1), 20210010.

6 N. Jiang, C. Yang, Y. Wang, X. Wang, J. Liu and Y. Liu, A Mn-based ternary NASICON-type $Na_{3.5}MnTi_{0.5}Cr_{0.5}(PO_4)_3$/C cathode for high-performance sodium-ion batteries, *Energy Storage Mater.*, 2023, **63**, 102978.

7 J. Gao, Y. Tian, Y. Mei, L. Ni, H. Wang, H. Liu, *et al.*, Robust NASICON-type iron-based $Na_4Fe_3(PO_4)_2(P_2O_7)$ cathode for high temperature sodium-ion batteries, *Chem. Eng. J.*, 2023, **458**, 141385.

8 J. Hou, M. Hadouchi, L. Sui, J. Liu, M. Tang, W. H. Kan, *et al.*, Unlocking fast and reversible sodium intercalation in NASICON $Na_4MnV(PO_4)_3$ by fluorine substitution, *Energy Storage Mater.*, 2021, **42**, 307–316.

9 M. Hadouchi, J. Hou, T. Koketsu, A. Lahmar and J. Ma, Fluorophosphates and fluorosulfates cathode materials: Progress towards high energy density sodium-ion battery, *Nano Res.*, 2024, **17**(3), 1427–1440.

10 R. Thirupathi, V. Kumari, S. Chakrabarty and S. Omar, Recent progress and prospects of NASICON framework electrodes for Na-ion batteries, *Prog. Mater. Sci.*, 2023, **137**, 101128.

11 Y. Li, M. Li, Z. Sun, Q. Ni, H. Jin and Y. Zhao, Recent advance on NASICON electrolyte in solid-state sodium metal batteries, *Energy Storage Mater.*, 2023, **56**, 582–599.

12 H. Li, W. Zhang, K. Sun, J. Guo, K. Yuan, J. Fu, *et al.*, Manganese-Based Materials for Rechargeable Batteries beyond Lithium-Ion, *Adv. Energy Mater.*, 2021, **11**(25), 1–35.

13 P. Hu, T. Zhu, C. Cai, X. Wang, L. Zhang, L. Mai, *et al.*, A High-Energy NASICON-Type $Na_{3.2}MnTi_{0.8}V_{0.2}(PO_4)_3$ Cathode Material with Reversible 3.2-Electron Redox Reaction for Sodium-Ion Batteries, *Angew. Chem.*, 2023, **135**(14), 1–9.

14 W. Zhang, H. Li, Z. Zhang, M. Xu, Y. Lai and S. L. Chou, Full Activation of Mn^{4+}/Mn^{3+} Redox in $Na_4MnCr(PO_4)_3$ as a High-Voltage and High-Rate Cathode Material for Sodium-Ion Batteries, *Small*, 2020, **16**(25), 1–8.

15 W. Zhou, L. Xue, X. Lü, H. Gao, Y. Li, S. Xin, *et al.*, $Na_xMV(PO_4)_3$ (M = Mn, Fe, Ni) Structure and Properties for Sodium Extraction, *Nano Lett.*, 2016, **16**(12), 7836–7841.

16 Q. Wang, C. Ling, J. Li, H. Gao, Z. Wang and H. Jin, Experimental and theoretical investigation of $Na_4MnAl(PO_4)_3$ cathode material for sodium-ion batteries, *Chem. Eng. J.*, 2021, **425**, 130680.

17 Y. Zheng, J. Liu, D. Huang, H. Chen and X. Hou, Prepare and optimize NASICON-type $Na4MnAl(PO_4)_3$ as low cost cathode for sodium ion batteries, *Surf. Interfaces*, 2022, **32**(June), 102151.

18 S. h. Luo, J. y. Li, S. Bao, Y. y. Liu and Z. Wang, $Na_3MnZr(PO_4)_3$: A High-Voltage Cathode for Sodium Batteries, *J. Electrochem. Soc.*, 2018, **165**(7), A1460–A1465.

19 Y. Cao, Y. Liu, D. Zhao, X. Xia, L. Zhang, J. Zhang, *et al.*, Highly Stable $Na_3Fe_2(PO_4)_3$@Hard Carbon Sodium-Ion Full Cell for Low-Cost Energy Storage, *ACS Sustain. Chem. Eng.*, 2020, **8**(3), 1380–1387.

20 R. Rajagopalan, B. Chen, Z. Zhang, X. L. Wu, Y. Du, Y. Huang, *et al.*, Improved Reversibility of Fe^{3+}/Fe^{4+} Redox Couple in Sodium Super Ion Conductor Type $Na_3Fe_2(PO_4)_3$ for Sodium-Ion Batteries, *Adv. Mater.*, 2017, **29**(12), 1605694.

21 Y. Liu, Y. Zhou, J. Zhang, Y. Xia, T. Chen and S. Zhang, Monoclinic phase $Na_3Fe_2(PO_4)_3$: synthesis, structure, and electrochemical performance as cathode material in sodium-ion batteries, *ACS Sustain. Chem. Eng.*, 2017, **5**(2), 1306–1314.

22 S. Qiu, X. Wu, M. Wang, M. Lucero, Y. Wang, J. Wang, *et al.*, NASICON-type $Na_3Fe_2(PO_4)_3$ as a low-cost and high-rate anode material for aqueous sodium-ion batteries, *Nano Energy*, 2019, **64**, 103941.

23 R. A. Shakoor, C. S. Park, A. A. Raja, J. Shin and R. Kahraman, A mixed iron-manganese based pyrophosphate cathode, $Na_2Fe_{0.5}Mn_{0.5}P_2O_7$, for rechargeable sodium ion batteries, *Phys. Chem. Chem. Phys.*, 2016, **18**(5), 3929–3935.

24 S. Wei, B. Mortemard de Boisse, G. Oyama, S. I. Nishimura and A. Yamada, Synthesis and Electrochemistry of $Na_{2.5}(Fe_{1-y}Mn_y)1.75(SO_4)_3$ Solid Solutions for Na-Ion Batteries, *ChemElectroChem*, 2016, **3**(2), 209–213.

25 Q. Zheng, H. Yi, X. Li and H. Zhang, Progress and prospect for NASICON-type $Na_3V_2(PO_4)_3$ for electrochemical energy storage, *J. Energy Chem.*, 2018, **27**, 1597–1617.

26 S. Chen, C. Wu, L. Shen, C. Zhu, Y. Huang, K. Xi, *et al.*, Challenges and Perspectives for NASICON-Type Electrode Materials for Advanced Sodium-Ion Batteries, *Adv. Mater.*, 2017, **29**(48), 1–21.

27 S. Sradhasagar, S. Mallick, A. Rath, S. Pati and A. Roy, Role of Fe^{3+} doping vis-à-vis secondary phases on the electrical transport of $LiTi_2(PO_4)_3$ solid electrolyte, *Mater. Today Commun.*, 2023, **35**, 105621.

28 Dspace, **http://dspace.nbuv.gov.ua/handle/123456789/49501**, accessed April 2024.

29 J. Carvajal FULLPROF: A Program for Rietveld Refinement and Pattern Matching Analysis, in *Abstracts of the Satellite Meeting on Powder Diffraction of the XV Congress of the IUCr*, Toulouse, France, 1990, p. 127.

30 K. Brandenburg and H. Putz, Diamond-crystal and molecular structure visualization crystal impact, *Rathausgasse*, 2006, **30**, 1997–2000.

31 I. D. Brown and D. Altermatt, Bond-Valence Parameters Obtained from a Systematic Analysis of the Inorganic Crystal Structure Database, *The bond file produced from the Inorganic Crystal*, 1985, pp. 244–247.

32 M. Hadouchi, N. Yaqoob, P. Kaghazchi, M. Tang, J. Liu, P. Sang, *et al.*, Fast sodium intercalation in $Na_{3.41}£_{0.59}FeV(PO_4)_3$: a novel sodium-deficient NASICON cathode for sodium-ion batteries, *Energy Storage Mater.*, 2021, **35**, 192–202.

33 F. Ejehi, S. P. H. Marashi, M. R. Ghaani and D. F. Haghshenas, The synthesis of NaSICON-type $ZrNb(PO_4)_3$ structure by the use of Pechini method, *Ceram. Int.*, 2012, **38**(8), 6857–6863.

34 S. Naqash, Q. Ma, F. Tietz and O. Guillon, $Na_3Zr_2(SiO_4)_2(PO_4)$ prepared by a solution-assisted solid state reaction, *Solid State Ionics*, 2017, **302**, 83–91.

35 C. J. Antony, A. Aatiq, C. Y. Panicker, M. J. Bushiri, H. T. Varghese and T. K. Manojkumar, FT-IR and FT-Raman study of Nasicon type phosphates, $ASnFe(PO_4)_3$ [A = Na_2, Ca, Cd], *Spectrochim. Acta, Part A*, 2011, **78**(1), 415–419.

36 J. Zhao, W. Yan, S. Li, S. Li, W. H. Wang and Y. Bai, Double-pinning effect assisting $Na4VMn(PO_4)_3$ with superior structural and electrochemical stabilization for sodium-ion batteries, *Nano Energy*, 2024, **119**, 109002.

37 H. Güler and F. Kurtuluș, A rapid synthesis of sodium titanium phosphate, $NaTi_2(PO_4)_3$ by using microwave energy, *Mater. Chem. Phys.*, 2006, **99**(2–3), 394–397.

38 V. S. Kurazhkovskaya, D. M. Bykov and A. I. Orlova, Infrared spectroscopy and structure of trigonal zirconium orthophosphates with lanthanides and actinides, *J. Struct. Chem.*, 2004, **45**(6), 966–973.

39 E. Kazakevičius, A. Kežionis, L. Žukauskaite, M. Barré, T. Šalkus, A. Žalga, *et al.*, Characterization of $Na_{1.3}Al_{0.3}Zr_{1.7}(PO_4)_3$ solid electrolyte ceramics by impedance spectroscopy, *Solid State Ionics*, 2015, **271**, 128–133.

40 J. F. Ortiz-mosquera, A. C. M. Rodrigues and A. M. Nieto-mu, The role of Al^{3+} on the microstructural and electrical properties of $Na_{1+x}Al_xTi_{2-x}(PO_4)_3$ NASICON glass-ceramics, *J. Alloys Compd.*, 2020, **820**, 1–10.

41 Y. Lee, B. U. Ye, D. K. Lee, J. M. Baik, H. K. Yu and M. H. Kim, The migration of alkali metal (Na^+, Li^+, and K^+) ions in single crystalline vanadate nanowires: Rasch-Hinrichsen resistivity, *Curr. Appl. Phys.*, 2019, **19**(4), 516–520.

42 F. Ma, E. Zhao, S. Zhu, W. Yan, D. Sun, Y. Jin, *et al.*, Preparation and evaluation of high lithium ion conductivity solution method, *Solid State Ionics*, 2016, **295**, 7–12.

43 H. Leng, J. Nie and J. Luo, Combining cold sintering and Bi_2O_3-activated liquid-phase sintering to fabricate high-conductivity Mg-doped NASICON at reduced temperatures, *J. Mater.*, 2019, **5**(2), 237–246.

44 S. Narayanan, S. Reid, S. Butler and V. Thangadurai, Sintering temperature, excess sodium, and phosphorous dependencies on morphology and ionic conductivity of NASICON $Na_3Zr_2Si_2PO_{12}$, *Solid State Ionics*, 2019, **331**, 22–29.

45 D. Tediashvili, G. Gečė, J. Pilipavičius, S. Daugėla, T. Šalkus, J. Juodkazytė, *et al.*, Synthesis, characterization, and degradation study of Mn-based phosphate frameworks ($Na_3MnTi(PO_4)_3$, $Na_3MnPO_4CO_3$, $Na_4Mn_3(PO_4)_2P_2O_7$) as aqueous Na-ion battery positive electrodes, *Electrochim. Acta*, 2022, **417**, 140294.

46 R. R. Samigullin, M. V. Zakharkin, O. A. Drozhzhin and E. V. Antipov, $Na_4VMn(PO_4)_3$ as Cathode Materials for Sodium-ion Batteries, *Energies*, 2023, **2**, 1–13.

47 F. Lalère, J. B. Leriche, M. Courty, S. Boulineau, V. Viallet, C. Masquelier, *et al.*, An all-solid state NASICON sodium battery operating at 200 C, *J. Power Sources*, 2014, **247**, 975–980.

48 G. Tippelt, Q. Stahl, A. Benisek and D. Rettenwander, Study on the structural phase transitions in as a model system research papers, *Acta Cryst.*, 2021, **2**, 10–22.